Ballistic response of needlepunched nonwovens

Citation for published version:
Martinez-Hergueta, F, Ridruejo, A, González, CA & LLorca, J 2022, Ballistic response of needlepunched nonwovens. in VV Silberschmidt (ed.), *Mechanics of Fibrous Networks.* Mechanics of Advanced Materials, Elsevier, pp. 241-261. https://doi.org/10.1016/B978-0-12-822207-2.00011-8

Digital Object Identifier (DOI):
10.1016/B978-0-12-822207-2.00011-8

Published In:
Mechanics of Fibrous Networks

Ballistic response of needlepunched nonwovens

F. Martínez-Hergueta[1], A. Ridruejo[2], C. González[2,3], J. LLorca[2,3]

[1] *School of Engineering, Institute for Infrastructure and Environment, The University of Edinburgh, William Rankine Building, EH9 3FG, Edinburgh, UK.*

[2] *Department of Materials Science, Universidad Politécnica de Madrid, E. T. S. de Ingenieros de Caminos. 28040 - Madrid, Spain.*

[3] *IMDEA Materials Institute, C/ Eric Kandel 2, 28906, Getafe, Madrid, Spain.*

Abstract

Needlepunched nonwoven fabrics manufactured with high strength fibres present lower stiffness and strength than their woven counterparts, but possess much higher deformability and energy absorption capacity, leading to excellent ballistic performance against small calibres. Although their potential advantages, very little is known about their deformation and fracture micromechanisms at the microscopic level and how they contribute to macroscopic mechanical properties such as ballistic limit. This lack of knowledge hinders the optimisation of their mechanical performance and also limits their implementation in structural applications. This chapter aims to review the response of needlepunched nonwovens subjected to ballistic impact. The experimental dynamic characterisation is conducted through a combination of Split-Hopkinson bar and impact tests. These procure the wave propagation phenomenon, the dominant deformation micromechanisms at high-strain rates and the residual velocity curves, including the ballistic limit. Additionally, a Finite Element Digital Twin is implemented in the software Abaqus/Explicit to explore the influence of the microstructure in the ballistic performance of the material. The numerical model is validated against previous experimental results and it is employed to analyse the potential of the material to improve the performance of targets such as dry woven fabrics and metal sheets. The addition of the nonwoven layer increases substantially the specific energy absorption capacity of the system, with a negligible increment of the total areal weight of the target.

Keywords: Needlepunched nonwoven, ballistic, Finite Element Digital Twin

1. Introduction

Fibre based dry fabrics are a lightweight solution for ballistic protection conventionally extended in the defence sector in a large variety of applications including soft vehicle and body armour [1, 2]. Depending on their architecture, the fabrics can be classified into two categories: wovens and nonwovens, see Fig. 1. Woven fabrics exhibit a homogeneous distribution where fibres are bundled in yarns weaved into regular patterns, while nonwovens present a random fibre network connected through local bonds consolidated by thermal fusion, chemical binding or mechanical entanglement [3]. These bonds determine the interaction between fibres and have a primary role in the deformation and ductility of the nonwoven. In particular, the needlepunched mechanical consolidation process results in a lower stiffness and strength (as well as processing cost), but much higher strain to failure than their woven counterparts, resulting in outstanding ductility and energy absorption capacity [4, 5, 6], with excellent ballistic performance against shrapnel and small calibres [7, 8], making nonwovens a perfect cushion layer for conventional dry woven fabric soft body armour shields [9, 10, 11, 12, 13].

Although the impact response of dry woven fabrics based on Kevlar and Dyneema fibres is detailed reported in the literature and their application is conventional in the defense sector [14, 15, 16], the technology readiness level of nonwoven fabrics is still immature and their applications are limited. It is possible to find in the literature a handful of examples focused on damage reduction of rear components [17, 18] or sandwich cores [19, 20], nevertheless, the lack of knowledge regarding the ballistic performance of needlepunched nonwovens hinders the development of predictive design tools and delays their wider implementation in the defence and transport sector. The mechanical response of needlepunched nonwovens subjected to quasi-static tensile loads is detailed reported in the literature [21, 22]. The stiffness of the material is directly proportional to the percentage of fibres oriented with the loading direction and the bond density. The manufacturing process can also induce an anisotropic mechanical response by introducing an heterogeneous connectivity between the fibres. Upon uniaxial deformation, the random fibre network evolves exhibiting progressive

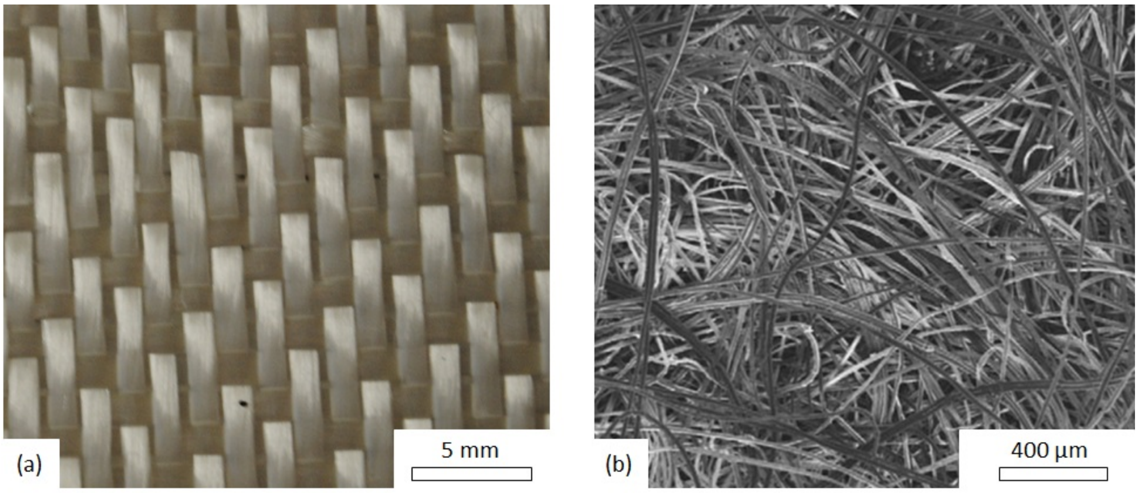

Figure 1: Ultrahigh molecular weight polyethylene fabrics. (a) 3 harness satin dry woven fabric composed of Dyneema SK65 fibre yarns and (b) needlepunched nonwoven fabric composed of Dyneema SK75 fibres.

fibre uncurling and rotation. This microstructural evolution leads to a non-linear response of the material, with increasing tangent stiffness with the deformation. The ductility at large strains is mainly controlled by frictional deformation micromechanisms such as fibre sliding, slippage and pull-out from the entanglement points (see previous chapter XX). These physical findings are the basis to develop sound, physically based, constitutive models to predict the mechanical response of needlepunched nonwovens [23], however, further efforts are needed to characterise the wave propagation phenomenon and determine the influence of high strain rates in the mechanical response of the material to extend the constitutive models to simulate impact events.

This chapter aims at reviewing the response of needlepunched nonwovens subjected to ballistic impact. A detailed experimental dynamic characterisation of the material is accomplished through Split-Hopkinson bar and impact tests. These procure the wave propagation phenomenon, the dominant deformation and failure micromechanisms at high-strain rates and the residual velocity curves, including the ballistic limit. Additionally, a Finite Element Digital Twin is developed in the software Abaqus/Explicit to explore potential applications in the defence and transport sectors. The numerical model is validated against experimental results and it is employed to analyse the potential of the material to improve the ballistic

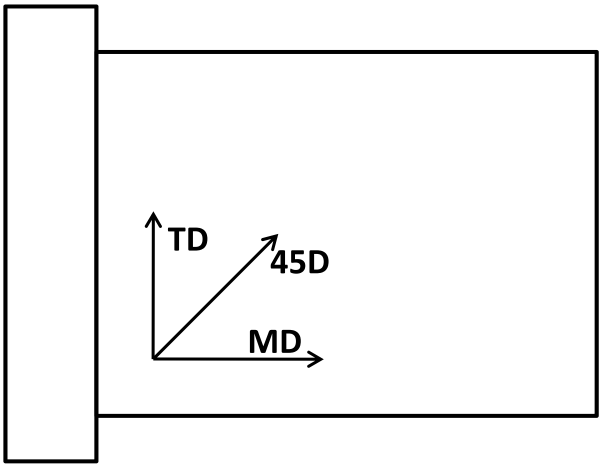

Figure 2: Main material orientations of the fabric. MD stands for machine direction and TD stands for transverse direction.

response of conventional targets such as dry woven fabrics and metal sheets. In both cases, the addition of the nonwoven layer increases substantially the specific energy absorption capacity of the targets with a minor increment of the total areal weight of the shield.

2. Experimental characterisation

2.1. Material

The two-dimensional needlepunched nonwoven is a DSM product commercialised under the trademark Fraglight NW201. It is composed of Dyneema SK75 ultrahigh molecular weight polyethylene fibres (UHMWPE) with an approximate length of $\approx$ 60 mm. The stochastic nature of the material results in a variable thickness of $\approx$ 1.5 to 2 mm and an areal weight of $\rho \approx$ 190-220 g/m^2. The batt is manufactured on a moving bed by continuous fibre deposition and mechanically entangled by oscillatory barbed needles [3]. This manufacturing process induces two principal material directions along the bed or machine direction (MD) and the transverse direction (TD), see Fig. 2. The difference in mechanical properties between perpendicular directions was pronounced, with higher stiffness and strength along the TD. The detailed quasi-static characterisation at different scales is available in previous chapter XX.

2.2. *Experimental techniques*

2.2.1. *In-plane dynamic tests*

The dynamic testing of the nonwoven fabric was conducted on a Split-Hopkinson Tensile Bar (SHTB) device with high sensitivity and long pulse duration specially designed for low-impedance fabrics with complex architectures and large Representative Volume Elements. The input and output bars comprised of Aluminium 7075-T6 alloy hollow tubes of 50.8 mm outer diameter, 1.651 mm wall thickness and 2.7 m in length. The pulse duration was $T \approx 1$ ms. The fabric was gripped by conical clamps allowing a maximum specimen width and gauge length of 35 x 35 mm^2. The samples were stretched at the orientation transverse to the roll direction (TD), the stiffest direction of the material, see Fig. 3(b). This experimental set-up resulted in strain rates of $\dot{\varepsilon} \approx 400$ s^{-1}, 4 orders of magnitude higher than the previously reported quasi-static characterisation [22]. Further details of this SHB equipment are available in [24, 25].

The bars were instrumented with three strain gauges, as in Fig. 3(a). Amplifiers and high frequency oscilloscopes were used to record the signal on the order of millivolts. The main outcomes were forces and velocities of the bars. The specimens were speckled with a random pattern and full-field displacement measurements were carried out via high-speed photography, employing an ultra-high-speed Kirana camera operated at 50.000 fps. 2D Digital Image Correlation analysis was performed using the commercial software Vic2D.

2.2.2. *Ballistic tests*

The ballistic experiments were conducted on specimens of 500 x 500 mm^2 fully clamped along their four edges on a metallic frame with a free surface of 350 x 350 mm^2. The projectiles were steel spheres of 5.5 mm in diameter (caliber 0.22) and 0.706 g of mass. They were propelled by a SABRE A1 + gas gun at velocities between 270 to 400m/s and impact energies between 25 and 55 J. The initial and residual velocities were monitored by a high-speed Phantom V12 camera with a resolution of 512 x 256 and 512 x 512 pixels and rate acquisition between 20.000 to 40.000 fps depending on the test duration. Further details of the experimental set-up are available in [26].

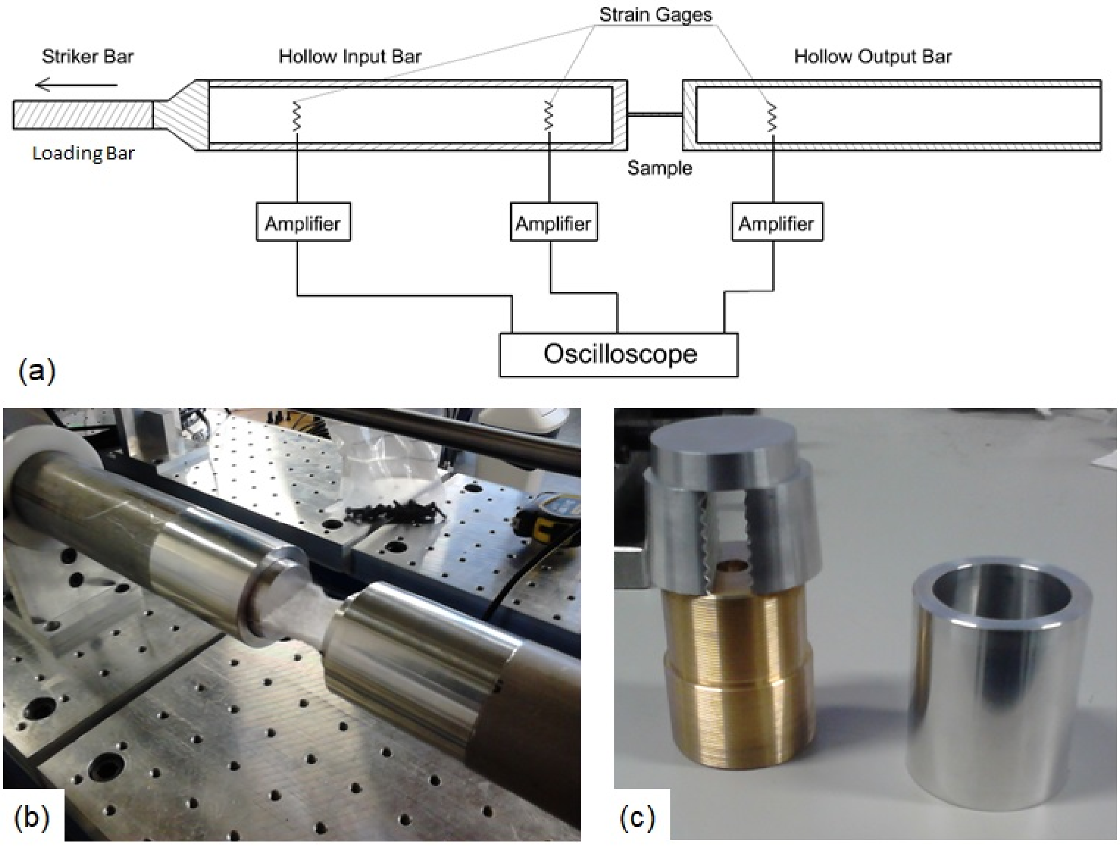

Figure 3: Split-Hopkinson tensile bar experimental set up. (a) Schematic of the different components of the SHTB, (b) gripped specimen between bar ends and (c) aluminium and brass components of the grips [25].

2.3. Experimental results

2.3.1. High-strain-rate tensile response

The tensile testing at high strain rates was conducted on the SHTB apparatus presented in Section 2.2.1. The forces were registered by the strain gauges while the deformation was obtained by Digital Image Correlation. The left hand side of Fig. 4 shows the evolution of the longitudinal deformation at different stages of the experiment, exhibiting large strain gradients across the specimen, in contrast to the characteristic homogeneous strain distributions obtained at quasi-static loading regimes before the onset of damage in this material [22]. At the initial stages of the loading process ($t = 0.4$ ms), the material acquired an oscillating deformation around the 20% as a result of the wave reflection process. After a

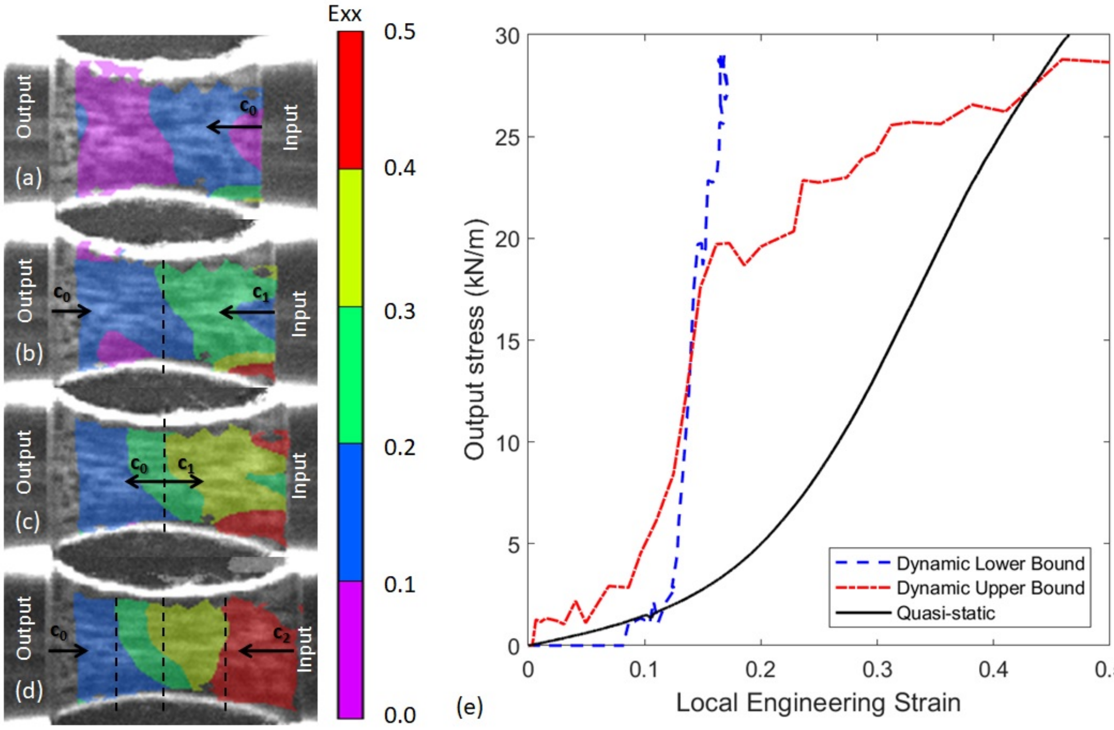

Figure 4: Evolution of the longitudinal strain ε_x and wave rebound phenomenon. (a) $t = 0.2$ ms, (b) $t = 0.4$ ms, (c) $t = 0.6$ ms, (d) $t = 0.9$ ms. (e) Output stress *vs.* local engineering strain at the output interface, the lower bound (blue dashed line) and input interface, the upper bound (red dashed line). Quasi-static stress-strain curve has been included for comparison purposes [25].

certain instant in time ($t = 0.6$ ms) the evolution of the strain nearby the output bar froze at a maximum value of 18% strain leading to a heterogeneous strain field across the specimen with an steep increment of deformation and damage localisation nearby the input bar, see Fig. 4(d). This strain gradients indicated a lack of dynamic force equilibrium between the bars during the whole duration of the experiment, usually observed during the first stages of the dynamic experiment before the input and output forces overlap [27].

The dynamic deformation induced progressive fibre straightening, rotation and sliding with the loading direction at microstructural level, as previously registered for quasi-static uniaxial deformation [22]. This evolution resulted in a non-linear pseudo-plastic mechanical response of the material with an inherent increment of the tangent stiffness. The fibre orientation distribution function was also proportional to the wave speed of the material that increased with the applied deformation. The initial fibre curvature and the random fibre orientation decreased the effective longitudinal propagation velocity, and the progressive fibre alignment increased the apparent wave speed of the fabric. Additionally, the magnitude of the tensile waves decreased with the distance with the input interface due to two different sources of mechanical dissipation: (i) the frictional nature of the deformation micromechanisms and (ii) the partial wave reflection at the entanglement points.

As a result of the variable stiffness and wave propagation velocity with the applied deformation, heterogeneous strain gradients appeared on the specimen during dynamic testing. The tensile pulse first propagated into the specimen with velocity c_0, see left hand side of Fig. 4. After a certain amount of time, the tensile pulse reached the output interface, meanwhile faster waves with a higher stress magnitude appeared at the input interface due to the non-linear increment of stiffness with fibre realignment ($c_1 > c_0$). Once the transmitted and reflected waves arrived at the same material point, they created a macromechanical interface with an impedance mismatch at both sides due to the differences in microstructural evolution, preventing the propagation of larger strain waves into the left side of the specimen. The reflections were repeated with waves of higher stress magnitude and velocity over the test duration ($c_2 > c_1$), generating additional mismatch fronts.

The output forces were analysed to determine the influence of the high strain rates in the mechanical response of the fabric. The Fig. 4(e) plots the output stress monitored by the strain gauge *vs.* the local longitudinal strains registered by DIC at the input and output interfaces. The lack of a constant strain over the specimen hindered the acquisition of a conventional stress-strain curve. These curves are compared against the quasi-static stress-strain constitutive relationship. A sudden increase in stiffness was registered, reaching a stress value of 30 kN/m within the range 15-17% deformation, which indicated a significant strain rate sensitivity of the frictional deformation micromechanisms. Further information is available in [25].

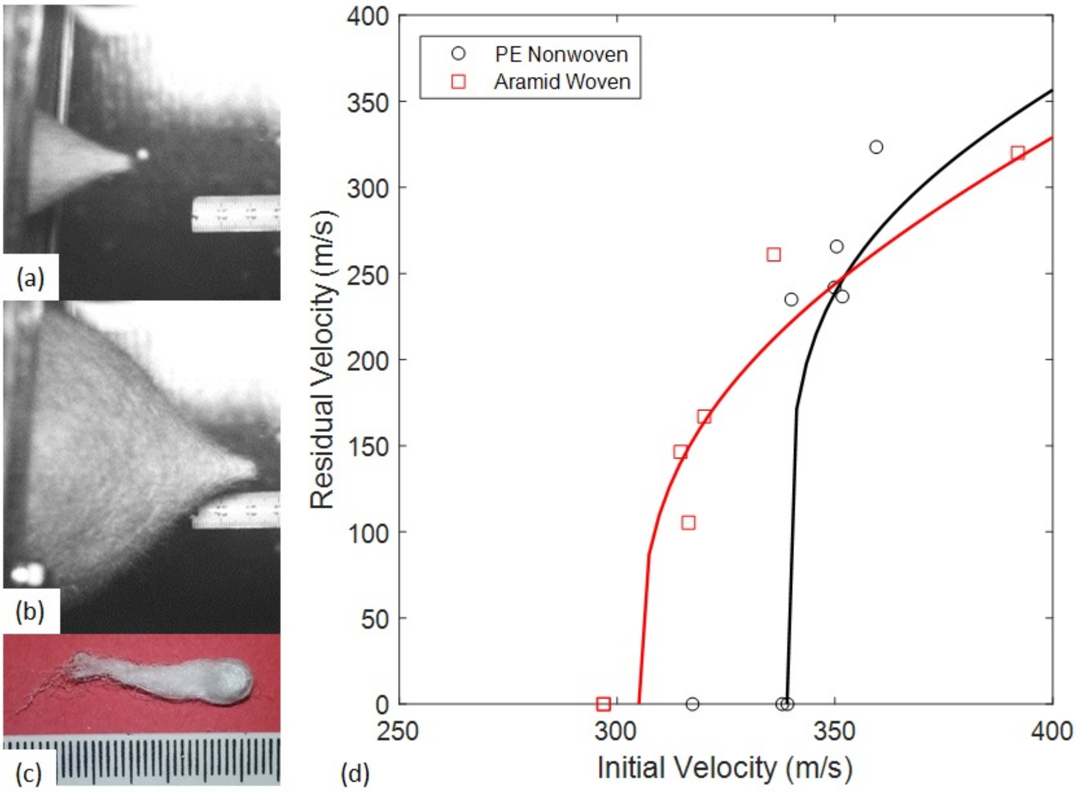

Figure 5: Deformation of the polyethylene nonwoven fabric during impact at the ballistic limit $v = 338$ m/s. (a) $t = 175$ μs. (b) $t = 1025$ μs. (c) Extracted fibres around the projectile after impact. (d) Residual velocity curves of the nonwoven fabric (1 layer with equivalent areal weight 200 g/m^2) and comparison with a conventional woven aramid laminate (4 layers with equivalent areal weight 922 g/m^2). The symbols stand for experimental results and the lines for eq. (1) [26].

2.3.2. Ballistic performance

The ballistic experimental campaign was conducted to evaluate the ballistic response of the material, obtain the residual velocity curve and identify the ballistic limit, v_{50}. Fig. 5 shows an example of the deformation of the fabric subjected to an impact velocity around the ballistic limit (v = 338 m/s). The differences in wave propagation velocities across perpendicular directions (MD and TD) resulted in an elliptical cross-section and the transverse wave that followed the deflection of the layer exhibited a cone profile. The needlepunched nonwoven absorbed the kinetic energy of the projectile by in-plane deformation. The load was transferred through the mechanical entanglements inducing fibre uncurling, rotation and sliding towards the impact point, as previously appreciated during quasi-static and dynamic uniaxial tensile testing. For impact velocities above the ballistic limit, large fibre pull-out and final tearing of the layer was registered, see Fig. 5(c). In all the cases, the damage was localised at the impact point and large strain gradients were exhibited, similar to the ones observed during the Split Hopkinson bar experiments. The thermal softening of the directly impacted fibres was also registered and validated through Differential Scanning Calorimetry. This resulted in a lower energy absorption capacity at velocities above the v_{50}. Further information is available in [26].

The residual velocity curve of the material is shown in Fig. 5(d). The experimental results were post-processed to obtained the least squares fitting with the Lambert equation,

$$V_{res} = (V_{ini}^n - V_{50}^n)^{1/n} \tag{1}$$

where V_{res} and V_{ini} are the residual and initial impact velocities, respectively. The ballistic response of the material was compared against the response of a conventional dry woven aramid target composed of 4 layers of Kevlar KM2 fibres with an equivalent areal weight of 920 g/m^2. The nonwoven exhibited a ballistic limit of 339 m/s and an energy absorption capacity of 40 J, 10 J higher than the maximum energy absorption capacity of the aramid protection, even if the nonwoven protection was four times lighter. This experimental campaign probes the advantage of nonwovens over woven against ballistic impact for small calibres and shrapnel.

3. Numerical simulation

3.1. Numerical implementation

A finite element model of the needlepunched nonwoven was implemented in the software Abaqus/Explicit to create a Digital Twin to predict the ballistic response of the material. The multiscale constitutive model presented in previous Chapter XXX was implemented as a VUMAT subroutine within the framework of large deformations taking as reference the unstressed state of the material. The detailed description of the model is available in

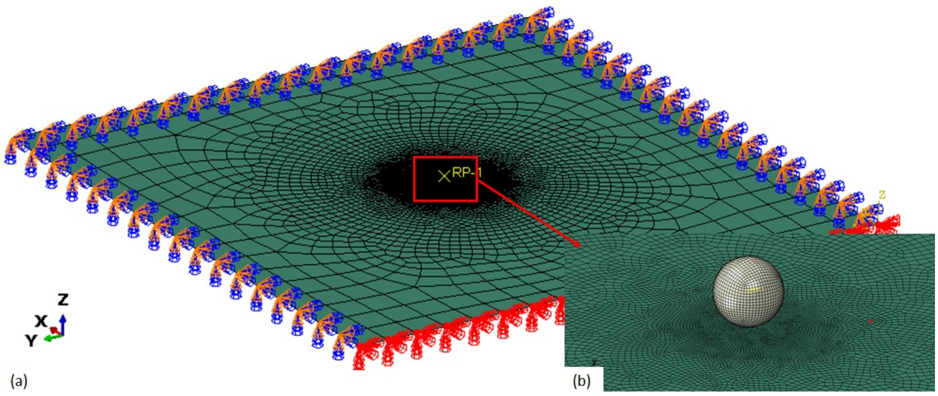

Figure 6: (a) Mesh strategy and boundary conditions and (b) mesh refinement at the impact point.

[23, 28]. The implementation for dynamic analysis incorporated one modification at Gauss point level, such that each mesodomain of the fibre network was described by 65 sets of fibres with different orientation instead of 33 to reduce the numerical instabilities. The strain rate dependency previously observed during the dynamic characterisation was accounted by two different material parameters; (i) the fibre pull-out length, L_{po}, that increased up to the total length of the fibre of 60 mm, in agreement with the full fibre pull-out registered experimentally, see Fig. 5(c), and (ii) the pull-out strength, σ_{po}, randomly defined withing the range [0.3 - 1.7] GPa, to fit the ballistic limit of the fabric. See Table XX in Chapter XX for reference. The same deletion criteria (average damage variable $D > 0.99$) as in previous quasi-static simulations was applied to replicate the penetration by fibre disentanglement of the target.

The clamped free area of the fabric of 350 x 350 mm^2 was discretised with reduced integration M3D4R membrane elements, with enhanced hourglass control and second order accuracy, see Fig. 6. The target was fully clamped along the four edges. The impact point was discretised with a fine mesh composed of elements of 1 mm^2, and a coarser mesh was implemented with the distance from the impact zone to decrease the number of degrees of freedom. The projectile was modelled as a solid rigid steel sphere of 5.5 mm in diameter and 7.85 g/cm^3. The tangential friction coefficient between the sphere and the fabric was set as 0.1.

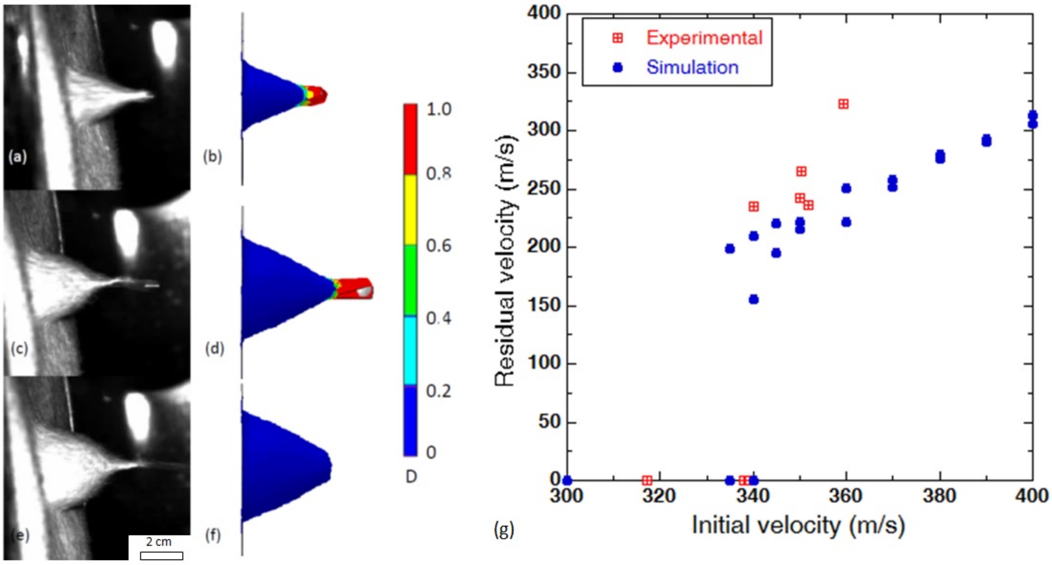

Figure 7: Correlation between the experimental deflection and the damage contour plot of the needlepunched nonwoven during an impact at 360 m/s. (a) and (b) t = 100 μs. (c) and (d) t = 175 μs and (e) and (f) t = 250 μs. The red color stands for the disentangled fabric. (g) Experimental and numerical residual velocity curves. Reproduced with permission from [28].

3.2. Validation

The performance of the Digital Twin was analysed to determine if it captured accurately the energy absorption mechanisms of the nonwoven material. The left hand side of Fig. 7 shows the numerical comparison of the experimental and numerical deflection of the layer during an impact above the ballistic limit, showing very good agreement in terms of damage prediction. An in-plane tensile wave stretched the layer towards the impact point, while the transverse wave captured the deflection with elliptical cross-section previously observed during the experimental campaign. The region of the material within the bounds of the in-plane longitudinal tensile wave dissipated the impact energy through the deformation mechanisms aforementioned; fibre uncurling, rotation and sliding. The model also predicted the strain gradients localised at the impact point and the fibre disentanglement resulting in tearing and penetration of the ply.

The Digital Twin also captured the energy absorption capacity of the material and the ballistic limit. Fig. 7(g) shows the residual velocity curves and compares the experimental and numerical residual velocities, V_{res}, as a function of the initial impact velocities, V_{ini}. The experimental scattering was reproduced by the stochastic definition of the pull-out strength as mentioned in Section 3.1. Although the model was able to capture the ballistic limit, it overestimated the energy absorption capacity above that threshold, as it did not considered the thermal softening of the Dyneema fibres registered during ballistic impact. Further information regarding the validation of the Digital Twin might be consulted in [28].

4. Case Study 1. Ballistic response of hybrid nonwoven/woven targets

Dry woven and nonwoven fabrics can be combined to create soft body armour protections with improved ballistic performance to arrest a large range of caliber sizes. The nonwoven is usually placed in the frontal face to act as cushion layer and enhance the load transmission into the woven fabric [18, 17, 29]. In this section we aim to investigate the synergistic contribution between the nonwoven and woven layers against impact, from an experimental and numerical point of view. A ballistic experimental campaign has been conducted to determine the ballistic limit and the energy absorption capacity of the hybrid target. The role of each layer at different stages of the impact process was ascertained using a Digital Twin, that provided separately information on kinetic and strain energy absorbed as function of time.

4.1. Materials

The Dyneema hybrid target was composed by a nonwoven (NW) layer and 4 rear harness satin woven fabrics (W) with stacking sequence $[NW/0_W/90_W/0_W/90_W]$. The areal density of the shield was 920 g/m^2, where each individual layer of the woven Dyneema fabric had an areal density of $\approx$ 180 g/m^2 and thickness of $\approx$ 0.5 mm. The full description of the experimental set-up which comprised a gas gun and high-speed camera is available in section 2.2.2. The size of the projectile (5.5 mm diameter) was approximately 4 times the width of the woven Dyneema yarns, easily promoting yarn sliding during ballistic impact due to the low friction coefficient of the Dyneema fibres. Further details of this experiment are available in [30].

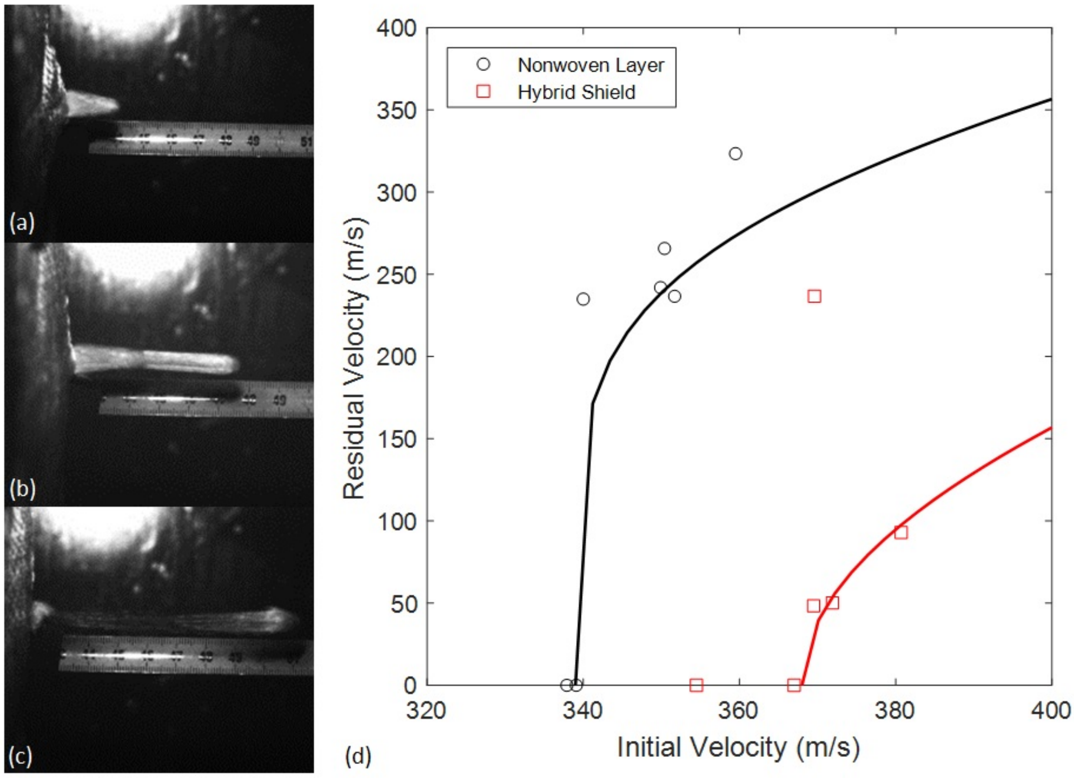

Figure 8: Deflection of the hybrid shield for an impact velocity of 370 m/s. (a) $t = 150$ μs. (b) $t = 600\mu$s. (c) $t = 1350$ μs. (d) Residual velocity curves of the hybrid shield (920 g/m^2) and comparison with the nonwoven layer (200 g/m^2) [30].

4.2. Experimental results

The impact response of the hybrid target is shown in Fig. 8 during an impact at 370 m/s. Initially, all layers deflected together until the yarns of the rear woven layers slid and the nonwoven got confined into the resulting gap. The confinement led to a high level of fibre alignment with the loading direction followed by a large percentage of extracted fibres. This resulted in a ductile response of the nonwoven layer with large deformation before final disentanglement, inducing a very high energy dissipation. The hybrid configuration presented superior energy absorption capacity when compared against the single nonwoven fabric. The residual velocity curves are shown in Fig. 8(d). The additional four layers of woven Dyneema increased the ballistic limit of the nonwoven by ≈ 30 m/s with an increment

Table 1: Elastic constants of the polyethylene SK65 yarns [32].

Density (ρ_f)	970 kg/m^3
Longitudinal elastic modulus (E_1)	95 GPa
Transverse elastic modulus (E_2)	9.5 GPa
Poisson's ratio (ν_{12})	0
Shear modulus (G_{12})	0.95 GPa

of 7 J of energy. It should be noted that the specific energy absorption capacity was higher for the single nonwoven considering the reduced weight, however, the areal weight of the hybrid shield was comparable to the previous dry woven aramid shield, see Fig. 5, and still exhibited a higher energy absorption capacity and ballistic limit than the previous [16, 1]. Furthermore, the addition of the nonwoven layer to the woven shield permitted the load transfer into the woven yarns and avoided the slippage failure mode previously observed during the ballistic impact of the single woven layers [30].

4.3. Numerical implementation

The analysis of the previous ballistic response was conducted by means of a Digial Twin based on a Finite Element Model. The nonwoven ply was implemented following the methodology exposed in previous Section 3.1, meanwhile, the woven fabric layers were modelled at mesoscale level, discretising the weaved yarns with C3D8 solid elements [31, 32], see Fig. 9. The elastic constants of the transversely isotropic yarn model are available in Table 1.

The nonwoven and the woven layers were combined to replicate the shield with stacking sequence [NW/0_W/90_W/0_W/90_W]. The dimensions of the nonwoven were set to 350 x 350 mm^2, meanwhile, the woven fabrics were limited to 100 x 100 mm^2 to reduce the computational cost. All fabrics were separated by a gap of 0.025 mm to avoid initial contact between layers and were constraint along the edges. The contact interaction between all the elements (the projectile, the yarns and the nonwoven) was modelled by a Coulomb friction algorithm with a friction coefficient of 0.0075. Further details are available in [30].

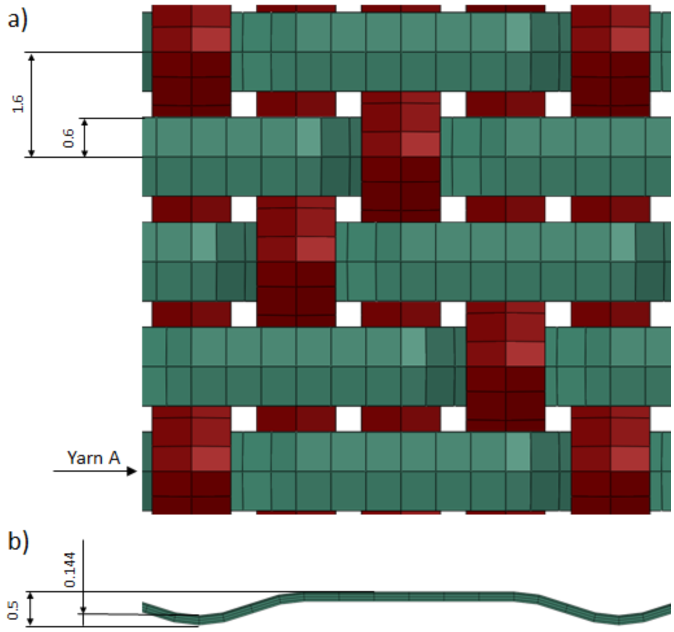

Figure 9: 3 harness satin pattern and mesoscale implementation of the woven layers. (a) Plan view. (b) Lateral view of yarn A. Measurements in mm [30].

4.4. Simulation results

The correlation between experimental and numerical results is shown in Fig. 10. A good agreement was found in terms of residual velocities and ballistic limit, such that the experimental results were obtained within the numerical scattering. Furthermore, the Digital Twin reproduced the improved behaviour of the hybrid shield with respect to the nonwoven and woven layers individually, and the complex interaction between the nonwoven and the weaved yarns. The left-hand side of Fig. 10 shows a comparison between the predicted and the experimental response at an impact velocity of 380 m/s. At the early stages of deflection ($t < 20$ μs) all the plies deflected together. The main energy absorption mechanisms at this stage were the kinetic and elastic energies transmitted to the rear woven layers. After yarn sliding and during the confinement stage, elastic deformation and kinetic energy transmitted to the nonwoven layer became the predominant dissipation mechanism. Final penetration of the shield occurred by extensive fiber disentanglement. The major contribution to the energy dissipation happened at the very early stages of the impact, where a reduction of the

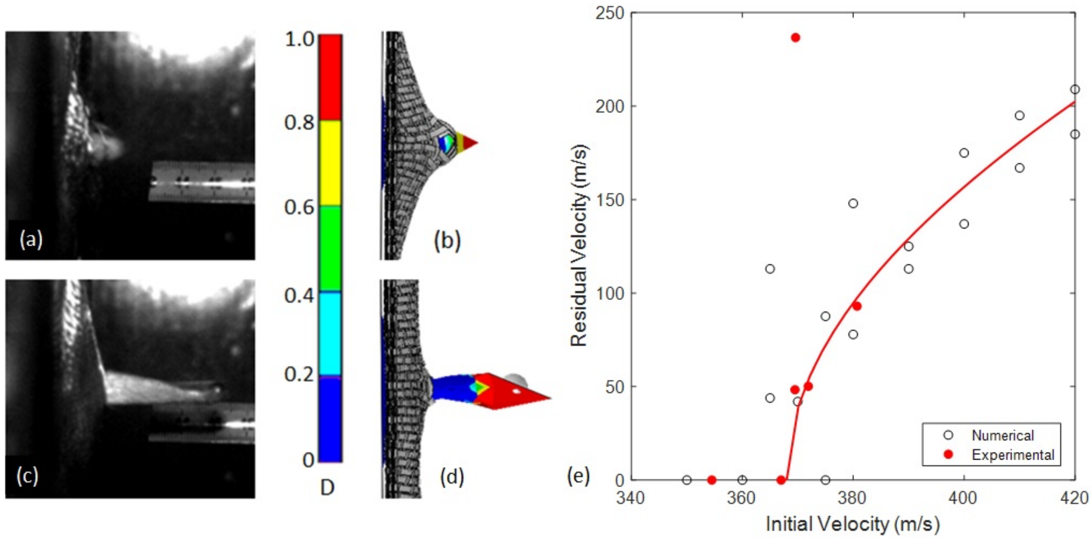

Figure 10: Correlation between the experimental deflection and the damage contour plot of the hybrid shield for an impact at 380 m/s. (a) and (b) t = 25 μs and (c) and (d) t = 150 μs. The red colour stands for the disentangled fibre network. (e) Comparison between experimental and predicted residual velocities as function of the impact velocity [30].

60% of the kinetic energy of the projectile was registered, 3 times higher than the energy absorbed by the baseline woven target. After the woven yarns slippage, an additional 20% of kinetic energy was dissipated due to the localised fibre pull-out. The hybrid configuration outperformed the capacity of each individual ply due to the synergistic interaction between layers. In particular, the nonwoven layer resulted in an optimal material to transfer the load to the adjacent woven layers, drastically increasing the energy absorption capacity of the woven target for these small calibers.

5. Case Study 2. Ballistic response of multi-layered metal/nonwoven shields

Dry fabrics can be also included in conventional hollow metallic components to improve the ballistic performance with a minimum increase of structural weight. The concept has been proven valid for turbine barriers, where the addition of Kevlar woven fabrics increased the ballistic performance against projectiles [33, 34]. This section aims to investigate the performance of a multilayered shield based on steel sheets, nonwovens and air gaps.

5.1. Materials

The nonwoven fabric was combined with a commercial bake hardening steel 260BH manufactured by Arcelor-Mittal [35]. The alloy is conventionally used in the automotive industry to manufacture components such as vehicle doors. It is designed specifically for structural applications and exhibits a high ductility, with high dent and impact resistance. The vehicle door was modelled as a hollow target with a total width of 80 mm constituted by two thin steel plates with 0.7 mm thickness with and equivalent areal weight of 11 kg/m^2. This configuration allow the incorporation of additional internal nonwoven fabrics in between the steel plates to increase the energy absorption capacity of the baseline structure. A maximum of 3 nonwoven layers was evaluated, regularly spaced with gaps of 10 mm and a distance of 30 mm with the steel plates, see Fig. 11. This resulted in an increment of 5.5% of the areal weight of the component, up to 11.6 kg/m^2.

5.2. Numerical implementation

A Digital Twin of the previous multilayered shield was implemented in the software Abaqus/Explicit to study the ballistic response of the target. The mechanical response of the nonwoven layers was implemented as described in previous section 3.1. The constitutive behaviour of the bake hardening steel was modelled as a standard isotropic elasto-plastic material available in the Abaqus/Explicit library based on the ductile failure criterion proposed in [36, 37, 38]. The model incorporated a linear hardening with a Von Mises yield surface which evolved as function of the applied plastic deformation, ε^{pl}, following the expression:

$$\sigma_y = \sigma_y^0 + H\varepsilon^{pl} \tag{2}$$

where σ_y^0 stood for the initial value of the yield strength and H for the hardening modulus. The onset of damage was determined by the ultimate strength of the material, σ_0. This value was combined with the hardening modulus to obtain the equivalent plastic strain to failure. Once the failure enveloped was overtaken, the material degradation was implemented by a phenomenological softening of the undamaged stress tensor, $\overline{\boldsymbol{\sigma}}$, such as:

$$\boldsymbol{\sigma} = (1 - d)\overline{\boldsymbol{\sigma}} \tag{3}$$

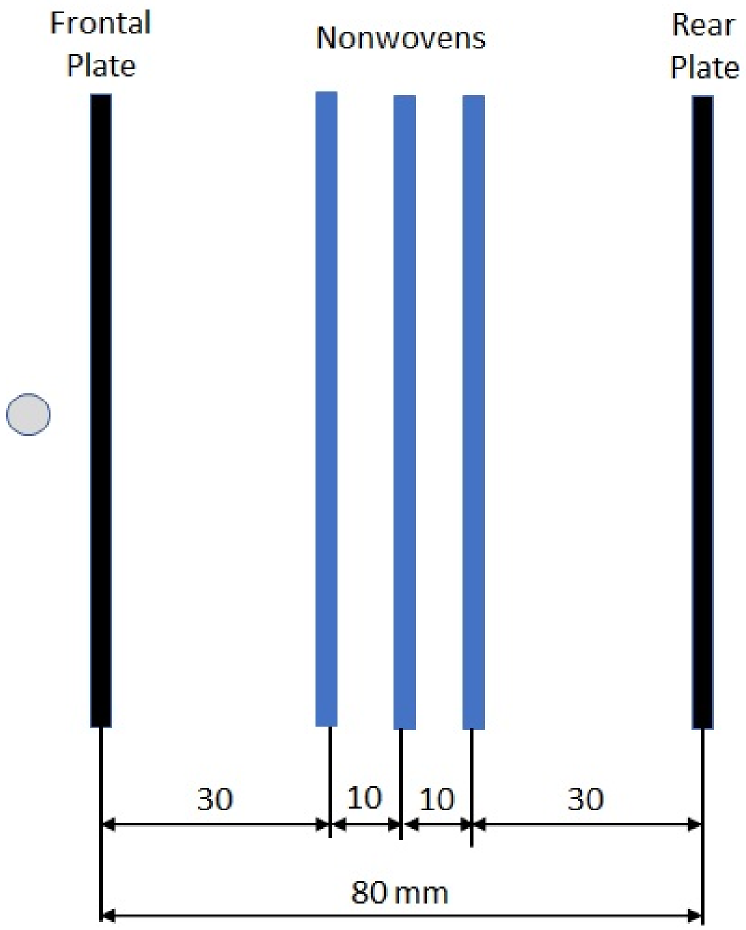

Figure 11: Multilayered configuration composed by 2 steel plates and 3 nonwoven plies. Measurements in millimeters.

where the damage variable, d, followed a conventional Lemaitre continuum damage model to ensure the dissipated energy was equal to the fracture toughness of the material, Γ, and avoid any size mesh dependency [39, 40]. Further information about the material model is available in [38] and material properties are summarized in Table 2. More details of the implementation are available in [41].

The door vehicle with the internal nonwoven layers was simplified as a 350 x 350 mm^2 target to reduce the computational cost. A higher mesh density was also defined around the impact point, with finite elements of 1 mm^2 area. All the layers were fully clamped on the edges during the impact simulation. The nonwoven layers were modelled using the

Table 2: Material parameters for Steel 260BH [41]

Density, ρ	7850 kg/m^3
Young's Modulus, E	200 GPa
Poisson's ratio, ν	0.27
Hardening Modulus, H	2.5 GPa
Ultimate Strength, σ_0	400 MPa
Yield Strength, σ_y^0	280 MPa
Strain to failure, ε_D^{pl}	0.3
Strain rate, $\dot{\varepsilon}^{pl}$	10^6
Triaxiality, ξ	0.8
Fracture toughness Γ	0.072 J/mm^2

approach in previous section 3.1, meanwhile, the thin steel plates were modelled with S4R shell elements, reduced integration, hourglass control and finite membrane strain. A rigid steel sphere of 5.5 mm in diameter as in previous ballistic studies was implemented to simulate the projectile. The penetration of the layers was reproduced by the deletion of the fully damaged elements, once the damage variable achieved the threshold $D > 0.99$. The contact between steel plates and nonwoven layers was implemented by a softened tangential contact behaviour with an sticking friction slope of κ= 0.001 and a friction coefficient μ=0.1.

5.3. Simulation results

The Digital Twin was able to reproduce the ballistic response of the multilayered shield, and the interaction between the layers. The right hand side of Fig. 12 shows the penetration sequence. Initially, the projectile pierced the frontal steel plate causing a minimum plastic deformation located at the impact point and hit the rest of the layers and rear metal plate, increasing the strain and kinetic energy absorbed by the system and decreasing the kinetic energy of the projectile. The progressive deformation induced damage on the nonwoven layers, nevertheless, final disentanglement was inhibited by the rear metal plate, that contributed structurally delaying the penetration of the layers and increasing the energy

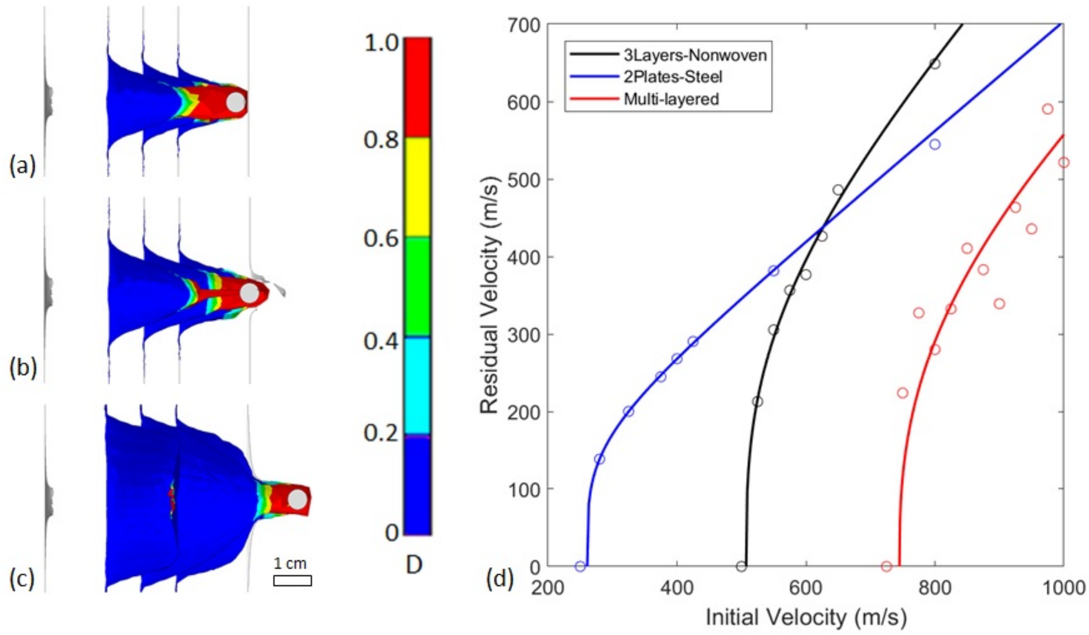

Figure 12: Ballistic response of the multi-layered shield impacted at 725 m/s. (a) t = 90 μs (b) t = 135 μs and (c) t = 225 μs. Contour plots of the damage variable. (d) Residual velocity curves for the multi-layered shield and comparison against the baseline configuration (2 plates of steel) and the 3 layers of nonwoven reinforcement [41].

absorbed by the target, see Fig.12(a). For impact velocities just below the ballistic limit, the penetration of the rear steel plate was predicted before the full nonwoven disentanglement took place, resulting in a similar confinement to the one appreciated in the hybrid woven/nonwoven shield, see Section 4.2. This confinement resulted in a high volume of fibre alignment, increasing the energy absorbed locally due to fibre pull-out.

The ballistic performance of the multi-layered component was compared in terms of energy absorption capacity against the predictions for its individual components; the steel plates and the nonwoven layers. Fig.12(d) compares the residual velocity curves. The steel plates with an equivalent weight of 11 kg/m^2 presented the lowest ballistic limit with a maximum energy absorption capacity of 19.5 J, characteristic of thin metallic plates. A large increment of energy absorption capacity was found for the 3 nonwoven layers, with an equivalent energy absorption capacity of 94.5 J. The multi-layered shield surpassed the ballistic performance of their individual components, with a maximum energy absorption capacity of 195.9 J, almost doubling the capacity of the sum of the previous. This represented a massive improvement of specific energy absorption capacity over a factor of 8 when compared against the conventional door vehicle with a minor increment of total areal weight of 5.5%. The large deformation of the nonwoven layers and their synergistic interaction with the rear metal sheet led to this outstanding improvement of ballistic performance.

6. Conclusions

The ballistic response of a Dyneema needlepunched nonwoven fabric composed by a random network of long fibres entangled through a mechanical process has been reviewed, with special focus on the main deformation and failure mechanisms, and their contribution to the overall energy absorption capacity of the material. The ballistic performance of the material was analysed in terms of residual velocity curves and ballistic limit. Additionally, a Digital Twin by means of a high fidelity Multiscale Finite Element Model was developed to provide further insight into physical events at microscale level that could not be revealed by high-speed imaging. The model was able to capture the main deformation micromechanisms such as fibre re-orientation and localisation of damage and was validated and calibrated against experimental data to ensure the robustness of the approach.

The in-plane dynamic response under high strain rates of the material was determined using a Split-Hopkinson tensile bar, specially designed for this purpose. The apparatus included a high-sensitivity output bar and had a long pulse duration to register the response of the low-impedance fibre network under large deformations. A high-speed camera registered the deformation micromechanisms under high strain rates, which comprised fibre straightening, rotation and sliding with the loading direction. These mechanisms were previously observed during the in-plane tensile quasi-static characterisation of the material. The main differences between the dynamic and the quasi-static loading regimes was the heterogeneous strain gradient developed at high-strain rates across the gauge length, not registered previously during the quasi-static analysis before the onset of damage. This heterogeneous strain field was a direct consequence of the dissipative nature of the frictional deformation processes and the internal impedance fronts originated in the material due the differences in microstructural evolution. As a result, the wave propagation phenomenon prevented the propagation of larger strain waves away from the loading point, resulting in large strain gradients located nearby the input edge. The frictional mechanisms between the entangled fibres presented a strong strain rate dependency with a significant increment of strain for low applied strains.

The ballistic response of the nonwoven layer was characterised by a combination of experimental and numerical analyses. The nonwoven layer was subjected to ballistic impact by a small steel sphere (5.5 mm in diameter) and presented outstanding energy absorption capacity compared to a conventional aramid woven target four times heavier than the novel nonwoven solution. During impact, the energy of the projectile was accommodated by the formation of a cone of deformed material with an elliptical cross-section due to the different wave propagation speed along material directions. The deformation was accommodated by the same micromechanisms observed during dynamic in-plane deformation, with a pronounced fibre rotation and re-alignment towards the impact point, and a sharp strain gradient with localised damage. The high ductility of the material resulted in its outstanding energy absorption capacity. The energy was dissipated by the tensile deformation of the fabric within the elliptical region defined by the wave speed of the material. The penetration of the ply occurred due to fibre disentanglement, with a large volume of fibres extracted from the layer at very large strain values.

The potential of the material to improve the ballistic response of conventional barriers was analysed with two additional case studies. In the first one, the nonwoven layer was used to improve the ballistic performance of a conventional Dyneema woven target, with a small ratio between projectile diameter and yarn width easily promoting yarn sliding and a poor ballistic performance. The nonwoven was positioned as a frontal layer to redistribute the load over the adjacent woven plies. As a result, a drastic increment of the ballistic limit and the energy absorption with respect to the original woven configuration was observed. During the first stages of the impact the energy was transmitted to the woven yarns through the nonwoven fabric, increasing by a factor of 3 the kinetic and strain energy absorbed by the woven shield. At a second stage, the projectile slipped through the yarns of the woven fabrics, however, the large ductility of the nonwoven resulted in a large fibre confinement with an additional energy absorption due to the large volume of extracted fibres.

The second case study focused on the improvement of the mechanical performance of conventional metal components in the transport sector such as a vehicle door. Three additional nonwoven layers were incorporated, separated by gaps of 10 mm. The hybrid system outperformed the performance of the steel plates and nonwoven layers, resulting in an outstanding energy absorption capacity about twice the sum of the energies dissipated by its individual components. Furthermore, the hybrid shield increased the energy absorption capacity of the baseline steel plates over a factor of 8, with a negligible increment of areal weight of a 5.5%.

The Digital Twin provided high-fidelity predictions of the different configurations in terms of ballistic limit and deformation mechanisms, with valuable insight regarding the evolution of energy absorption for each component of the shields. It has been proven a useful numerical tool that could be used in future design and optimisation tasks, however, the current approach to simulate the ballistic response of needlepunched nonwoven fabrics presents certain limitations and challenges that still need to be addressed. In particular, (i) the implementation of the strain rate dependency of the material is phenomenological and has been fitted against experimental results due to the lack of a high-strain-rate stress-strain relationship; (ii) the wave propagation phenomenon of the fibre network could not be accurately represented by the continuous mesodomain, so the simulations could not replicate the scattering and dissipation observed during the Slip Hopkinson bar experiments and (iii) a thermo-mechanical constitutive model needs to be implemented to capture the thermal softening of the fibres during ballistic impact.

This chapter demonstrates that the Dyneema needlepunched nonwoven fabric presents a lightweight solution to arrest small fragments, providing a low-cost alternative to improve the ballistic performance of conventional shields. As a result, it is possible to improve the ballistic performance of conventional civil automotive and aerospace components without penalising the fuel consumption to protect passengers against shrapnel. The nonwoven layer can be also incorporated into soft-body armour protections without reducing the users comfort, at a minimal increment of areal weight.

7. Acknowledgement

This research was supported by The Royal Society through the grant [RGS/R2/180091] and the Start-up funding for recently appointed lectures of The University of Edinburgh. The collaboration of Mr J. Vila-Ortega, Mr S. Carter, Dr F. Gálvez, Dr A. Pellegrino and Prof Nik Petrinic, are gratefully acknowledged.

References

[1] Mulat Alubel Abtew, Francois Boussu, Pascal Bruniaux, Carmen Loghin, and Irina Cristian. Ballistic impact mechanisms-a review on textiles and fibre-reinforced composites impact responses. *Composite Structures*, page 110966, 2019.

[2] Unsanhame Mawkhlieng, Abhijit Majumdar, and Animesh Laha. A review of fibrous materials for soft body armour applications. *RSC Advances*, 10(2):1066–1086, 2020.

[3] S. J. Russell. *Handbook of nonwovens*. The Textile Institute. Woodhead Publishing, 2007.

[4] Roy C. Laible and Malcolm C. Henry. A review of the development of ballistic needle-punched felts. Technical report, No. C/PSEL-TS-167. Clothing and Personal Life Support Equipment Laboratory. U.S. Army Natick Laboratories, 1969.

[5] S.J. Russell, A. Pourmohammadi, I. Ezra, and M. Jacobs. Formation and properties of fluid jet entangled HMPE impact resistant fabrics. *Composites Science and Technology*, 65(6):899–907, 2005.

[6] G. A. Thomas. Non-woven fabrics for military applications. In *Military Textiles*, pages 44–47. The Textile Institute. Woodhead Publishing, 2008.

[7] Thomas W. Ipson and Edward P. Wittrock. Response of non-woven synthetic fiber textiles to ballistic impact. Technical report, No. TR-67-8-CM. Denver Research Institute, 1966.

[8] Howard L Thomas, Ashok Bhatnagar, and Lori L. Wagner. Needle-Punched Non-Woven for High Fragment Protection. In *14th International Conference of Composite Materials*, San Diego, California, 2003.

[9] S. H. Lee and T. J. Kang. Mechanical and Impact Properties of Needle Punched Nonwoven Composites. *Journal of Composite Materials*, 34(10):816–840, May 2000.

[10] Jia-Horng Lin, Chan-Hung Hsu, and Hsien-Hui Meng. Process of preparing a nonwoven/filament/woven-fabric sandwich structure with cushioning effect of ballistic resistance. *Fibres & Textiles in Eastern Europe*, 13:43–47, 2005.

[11] P Rama Subba Reddy, T Sreekantha Reddy, I Srikanth, Juhi Kushwaha, and V Madhu. Development of cost effective personnel armour through structural hybridization. *Defence Technology*, 2019.

[12] Ruosi Yan, Qianyu Zhang, Bao Shi, Zhigang Qin, Sainan Wei, and Lixia Jia. Investigating the integral-structure of hrbp/chp/cf consisting of non-woven flexible inter/intra-ply hybrid composites: compression, puncture-resistance, electromagnetic interference shielding effectiveness. *Composite Structures*, page 112501, 2020.

[13] GA Thomas. Non-woven fabrics for military applications. *Military textiles*, pages 17–48, 2008.

[14] D Naik, S Sankaran, B Mobasher, S Rajan, and J Pereira. Development of reliable modeling methodologies for fan blade out containment analysis. Part I: Experimental studies. *International Journal of Impact Engineering*, 36(1):1–11, 2009.

[15] Philip M. Cunniff. An Analysis of the System Effects in Woven Fabrics Under Ballistic Impact. *Textile Research Journal*, 62(9):495–509, 1992.

[16] Ala Tabiei and Gaurav Nilakantan. Ballistic Impact of Dry Woven Fabric Composites: A Review. *Applied Mechanics Reviews*, 61(1):010801–1–13, 2008.

[17] Chia Chang Lin, Chao Chiung Huang, You Liang Chen, Ching Wen Lou, Chin Mei Lin, Chan Hung Hsu, and Jia Horng Lin. Ballistic-resistant stainless steel mesh compound nonwoven fabric. *Fibers and Polymers*, 9(6):761–767, 2009.

[18] C. C. Lin, C. M. Lin, C. C. Huang, C. W. Lou, H. H. Meng, C. H. Hsu, and J. H. Lin. Elucidating the Design and Impact Properties of Composite Nonwoven Fabrics with Various Filaments in Bulletproof Vest Cushion Layer. *Textile Research Journal*, 79(3):268–274, 2009.

[19] Jia Horng Lin, Chan Hung Hsu, and Hsien Hui Meng. Process of Preparing a Nonwoven / Filament / Woven-Fabric Sandwich Structure with Cushioning Effect of Ballistic Resistance. *Fibres & Textiles*, 13(4(52)):43–47, 2005.

[20] Amir Shahdin, Laurent Mezeix, Christophe Bouvet, Joseph Morlier, and Yves Gourinat. Fabrication and mechanical testing of glass fiber entangled sandwich beams: A comparison with honeycomb and foam sandwich beams. *Composite Structures*, 90(4):404–412, 2009.

[21] S. Chocron, A. Pintor, D. Cendón, C. Roselló, and V. Sanchez-Galvez. Characterization of Fraglight non-woven Felt and Simulation of FSP's Impact in it. Technical report, Technical University of Madrid, 2002.

[22] F. Martínez-Hergueta, A. Ridruejo, C. González, and J. LLorca. Deformation and energy dissipation mechanisms of needle-punched nonwoven fabrics: A multiscale experimental analysis. *International Journal of Solids and Structures*, 64:120–131, 2015.

[23] F. Martínez-Hergueta, A. Ridruejo, C. González, and J. LLorca. A multiscale micromechanical model of needlepunched nonwoven fabrics. *International Journal of Solids and Structures*, 96:81–91, 2016.

[24] R. Gerlach, C. Kettenbeil, and N. Petrinic. A new split Hopkinson tensile bar design. *International Journal of Impact Engineering*, 50:63–67, 2012.

[25] F. Martínez-Hergueta, A. Pellegrino, A. Ridruejo, N. Petrinic, C. Gonzalez, and J. LLorca. Dynamic tensile testing of needlepunched nonwoven fabrics. *Applied Sciences*, 10(15):5081, 2020.

[26] F. Martínez-Hergueta, A. Ridruejo, F. Gálvez, C. González, and J. LLorca. Influence of fiber orientation on the ballistic performance of needlepunched nonwoven fabrics. *Mechanics of Materials*, 94:106–116, 2016.

[27] F Martínez-Hergueta, D Ares, A Ridruejo, J Wiegand, and N Petrinic. Modelling the in-plane strain rate dependent behaviour of woven composites with special emphasis on the non-linear shear response. *Composite Structures*, 210:840–857, 2019.

[28] F. Martínez-Hergueta, A. Ridruejo, C. González, and J. Llorca. Numerical simulation of the ballistic response of needle-punched nonwoven fabrics. *International Journal of Solids and Structures*, 106:56–67, 2017.

[29] Hasam Basri Kocer. *Laminated and hybrid soft armor systems for ballistic applications*. PhD thesis, Auburn University, 2007.

[30] F. Martínez-Hergueta, A. Ridruejo, C. González, and J. LLorca. Ballistic performance of hybrid nonwoven/woven polyethylene fabric shields. *International Journal of Impact Engineering*, 111:55–65, 2018.

[31] Sidney Chocron, Eleonora Figueroa, Nikki King, Trenton Kirchdoerfer, Arthur E. Nicholls, Erick Sagebiel, Carl Weiss, and Christopher J. Freitas. Modeling and validation of full fabric targets under ballistic impact. *Composites Science and Technology*, 70(13):2012–2022, 2010.

[32] Sidney Chocron, Trenton Kirchdoerfer, Nikki King, and Christopher J. Freitas. Modeling of Fabric Impact With High Speed Imaging and Nickel-Chromium Wires Validation. *Journal of Applied Mechanics*, 78(5):051007, 2011.

[33] Donald A Shockey, David C Erlich, and Jeffrey W Simons. Lightweight Fragment Barriers for Commercial Aircraft. *18Th International Symposium on Ballistics*, pages 15–19, 1999.

[34] Z. Stahlecker, B. Mobasher, S. D. Rajan, and J. M. Pereira. Development of reliable modeling methodologies for engine fan blade out containment analysis. Part II: Finite element analysis. *International Journal of Impact Engineering*, 36(3):447–459, 2009.

[35] ArcelorMittal. Bake hardening steels, 2018.

[36] H Hooputra, H Gese, H Dell, and H Werner. A comprehensive failure model for crashworthiness simulation of aluminium extrusions. *International Journal of Crashworthiness*, 9(5):449–464, 2004.

[37] Ravi Kiran and Kapil Khandelwal. A triaxiality and lode parameter dependent ductile fracture criterion. *Engineering Fracture Mechanics*, 128:121–138, 2014.

[38] Dassault Systemes. *Abaqus 6.12 User's manual.* 2012.

[39] Jean Lemaitre. *A course on damage mechanics.* Springer Science & Business Media, 2012.

[40] Zdenek P Bazant and Jaime Planas. *Fracture and size effect in concrete and other quasibrittle materials*, volume 16. CRC press, 1997.

[41] J. Vila-Ortega, A. Ridruejo, and F. Martínez-Hergueta. Multiscale numerical optimisation of hybrid metal/nonwoven shields for ballistic protection. *International Journal of Impact Engineering*, 138:103478, 2020.